Molecular Cancer Therapeutics

Combined MEK and BCL-2/X$_L$ Inhibition Is Effective in High-Grade Serous Ovarian Cancer Patient–Derived Xenograft Models and BIM Levels Are Predictive of Responsiveness

Claudia Iavarone[1], Ioannis K. Zervantonakis[1], Laura M. Selfors[1], Sangeetha Palakurthi[2], Joyce F. Liu[3], Ronny Drapkin[4], Ursula A. Matulonis[3], Dorothy Hallberg[5], Victor E. Velculescu[5], Joel D. Leverson[6], Deepak Sampath[7], Gordon B. Mills[8], and Joan S. Brugge[1]

Abstract

Most patients with late-stage high-grade serous ovarian cancer (HGSOC) initially respond to chemotherapy but inevitably relapse and develop resistance, highlighting the need for novel therapies to improve patient outcomes. The MEK/ERK pathway is activated in a large subset of HGSOC, making it an attractive therapeutic target. Here, we systematically evaluated the extent of MEK/ERK pathway activation and efficacy of pathway inhibition in a large panel of well-annotated HGSOC patient–derived xenograft models. The vast majority of models were nonresponsive to the MEK inhibitor cobimetinib (GDC-0973) despite effective pathway inhibition. Proteomic analyses of adaptive responses to GDC-0973 revealed that GDC-0973 upregulated the proapoptotic protein BIM, thus priming the cells for apoptosis regulated by BCL2-family proteins. Indeed, combination of both MEK inhibitor and dual BCL-2/X$_L$ inhibitor (ABT-263) significantly reduced cell number, increased cell death, and displayed synergy in vitro in most models. In vivo, GDC-0973 and ABT-263 combination was well tolerated and resulted in greater tumor growth inhibition than single agents. Detailed proteomic and correlation analyses identified two subsets of responsive models—those with high BIM at baseline that was increased with MEK inhibition and those with low basal BIM and high pERK levels. Models with low BIM and low pERK were nonresponsive. Our findings demonstrate that combined MEK and BCL-2/X$_L$ inhibition has therapeutic activity in HGSOC models and provide a mechanistic rationale for the clinical evaluation of this drug combination as well as the assessment of the extent to which BIM and/or pERK levels predict drug combination effectiveness in chemoresistant HGSOC.

Introduction

High-grade serous ovarian cancer (HGSOC) is the most commonly diagnosed subtype of ovarian cancer and accounts for the majority of deaths from this disease (1, 2). Despite an initial response to platinum-based chemotherapy regimens, most patients with late-stage disease will experience cycles of relapse and development of treatment resistance ultimately leading to death. Improvement of HGSOC survival has been minimal over the past decade (3, 4). Therefore, the identification of new effective therapies and validated predictive biomarkers for patient selection represents an urgent, unmet clinical need.

The identification of targetable genetic drivers for HGSOC has been difficult due to the fact that somatic point mutations in oncogenes or tumor suppressors other than *TP53* are relatively uncommon in HGSOC. Instead, HGSOC is largely characterized by chromosomal instability with a large burden of copy-number gains and losses (5, 6). Genetic and proteomic characterization of HGSOC has identified aberrantly activated protumorigenic signaling pathways that represent attractive targets for therapeutic intervention (7, 8). However, the effectiveness of any single targeted therapy might be limited by the ability of tumor cells to develop adaptive mechanisms of resistance (9). This possibility is particularly true in HGSOC due to its genomic complexity (10–13). Thus, one promising approach is to identify and block adaptive responses to targeted agents through rationally designed combination therapies that can anticipate and overcome drug resistance (14).

The RAS/MEK/ERK pathway is frequently activated in HGSOC through copy-number alterations in key members of the pathway,

[1]Department of Cell Biology, Ludwig Center at Harvard, Harvard Medical School, Boston, Massachusetts. [2]Belfer Institute for Applied Cancer Res, Dana-Farber Cancer Institute, Boston, Massachusetts. [3]Department of Medical Oncology, Dana-Farber Cancer Institute, Boston, Massachusetts. [4]Penn Ovarian Cancer Res Center, Department of Obstetrics and Gynecology, University of Pennsylvania School of Medicine, Philadelphia, Pennsylvania. [5]The Sidney Kimmel Comprehensive Cancer Center, Johns Hopkins University School of Medicine, Baltimore, Maryland. [6]Oncology Development, AbbVie, Inc., North Chicago, Illinois. [7]Translational Oncology, Genentech, South San Francisco, California. [8]Department of Systems Biology, The University of Texas MD Anderson Cancer Center, Houston, Texas.

Corresponding Author: Joan S. Brugge, Harvard Medical School, 240 Longwood Avenue, Building C1, Room 513, Boston, MA 02115. Phone: 617-432-3974; Fax: 617-432-3969; E-mail: joan_brugge@hms.harvard.edu

©2019 American Association for Cancer Research.

AACR

including *NF1* deletions or gene breakages, and *KRAS* and *BRAF* amplifications (5, 6, 15). In addition, proteomic analyses of patient tumors have revealed that a subset of HGSOC exhibit MEK pathway activation as measured by the levels of phosphorylated forms of key nodes of the pathway, such as phospho-ERK (pERK). MEK pathway activation has also been implicated as an independent prognostic factor and predictor of early platinum-resistant relapse (16–18). These findings implicate the MEK/ERK pathway as a target in HGSOC.

MEK inhibition has been evaluated as a therapeutic strategy in several tumor types characterized by activating mutations in *KRAS* or *BRAF* such as melanoma but also including low-grade serous ovarian cancer (LGSOC; refs. 19–21). The modest clinical activity of MEK inhibitors as single agents in these studies is, at least in part, attributable to activation of compensatory survival pathways that lead to cell adaptation and drug resistance (22, 23). Of note, clinical responses were observed in both wild-type and mutant *KRAS* or *BRAF* tumors in a phase II clinical trial of the MEK inhibitor selumetinib in LGSOCs (24), suggesting that MEK inhibition can be effective in tumor types such as HGSOC that lack strong oncogenic drivers of this pathway. Despite the growing evidence of activation of the MEK pathway in HGSOC and its potential as a therapeutic target in this disease, a comprehensive assessment of MEK inhibitors and the adaptive responses they induce remains to be addressed in robust preclinical models of HGSOC.

Preclinical studies of therapeutic agents for HGSOC have largely relied on established ovarian cancer cell lines as model systems. However, significant differences in the molecular profiles have been reported between the most commonly used ovarian cancer cell lines and HGSOC tumors (25), calling into question the suitability of many of these lines as clinically relevant models for HGSOC. Alternatively, patient-derived xenografts (PDX) faithfully recapitulate the tumor of origin with respect to clinical pathology, degree of genetic heterogeneity and, importantly, response patterns to therapeutic regimens (26–28). Thus, PDXs represent a valuable clinical tool to assess efficacy of novel targeted therapies and identify predictive biomarkers to guide patient selection.

Here, we evaluated the effect of inhibiting the MEK/ERK signaling pathway in preclinical PDX models of HGSOC and identified a drug combination that exploited an adaptive response to MEK/ERK inhibition that primed cells for inhibition of BCL-2 and BCL-X$_L$. In addition, we utilized detailed proteomic and correlation analyses to define markers that correlate with drug combination sensitivity in different subsets of PDX models.

Materials and Methods

In vitro drug studies

Ascites cells were harvested from PDX models and were allowed to recover for 4 days *in vitro* in primary ovarian growth medium previously described (29). Cells were seeded in 96-well plates in MCDB105 + M199 medium, supplemented with 2% HI-FBS and 1% penicillin/streptomycin. Cells were treated with the indicated doses of GDC-0973, ABT-263, PD0325901, or MEK162 for 96 hours. Dose-response experiments were performed starting from a drug dose of 3 μmol/L followed by 3-fold serial dilutions for five dose ranges (dose range, 0.03–3 μmol/L). In the drug combination studies, the same dose range was used, and the two drugs were combined at 1:1 ratio. DMSO was used as control. At the end of

the treatment period, the relative cell number was determined by luciferase assay. D-luciferin (Fisher Scientific) was added to the cells in the 96-well plate, cells were incubated for 3 minutes at room temperature, and luciferase signal was measured using bioluminescence imaging (Envision 3). To determine growth rate, a parallel plate was read on the day of drug addition to calculate the luciferase signal before treatment (Day 0). For cell death analysis, after 96 hours of treatment, cells were incubated with NucGreen dye (Invitrogen) to identify dead cells, and the 96-well plate was read on a laser scanning cytometer (TTP Lab-Tech). The percentage of cell death was calculated by dividing the number of dead cells (green) by total cells (red plus green). Dose-response curves were generated in GraphPad Prism by plotting the relative cell number (normalized to the DMSO-treated condition 96 hours after drug treatment) for each drug concentration. IC$_{50}$ was determined from dose-response curves using GraphPad Prism by fitting a four-parameter, variable slope dose-response curve. A Bliss-independence model was used to evaluate combination effects. The Bliss expectation was calculated with the equation $(A + B) - A \times B$, in which A and B are the fractional growth inhibitions induced by agents A (i.e., GDC-0973) and B (i.e., ABT-263) at a given dose, respectively. The difference between the Bliss expectation and the observed growth inhibition induced by the combination of agents A and B at the same dose is the Bliss excess and is indicated as Bliss score. Genentech and AbbVie provided the compounds GDC-0973 and ABT-263, respectively. The compounds MEK162, PD0325901, and Z-VAD-FMK were purchased from Selleckchem. The established ovarian cell lines OVCAR3, OV90, OAW28, OVCAR8, OVSAHO, OVCAR5, TKYNU, JHOM1, and RMUGS were obtained from Dr. Dennis Slamon (UCLA) and were maintained in MCDB105/M199 medium supplemented with 10% HI-FBS and 1% penicillin/streptomycin (Invitrogen). Cell lines were reauthenticated using STR profiling. The *in vitro* drug dose-response experiments for these cell lines were performed as described for the PDX models. PDX models and established ovarian cancer cell lines tested negative for *Mycoplasma* contamination using luminescence assay.

In vivo PDX studies

All mouse studies were conducted through Institutional Animal Care and Use Committee (IACUC)–approved animal protocols in accordance with Harvard Medical School institutional guidelines. For drug efficacy studies, 8- to 10-week-old female NSG mice (Jackson labs) were injected intraperitoneally with approximately 5×10^6 cells/200 μL of PBS. Tumor burden was monitored using bioluminescence imaging (BLI; IVIS Lumina) 1–3 weeks after tumor cell injections. Mice were randomized based on BLI into four groups of eight mice each and were treated by oral gavage daily with GDC-0973 (7.5 mg/kg) or ABT-263 (100 mg/kg), or the combination of these drugs at the indicated doses. We used our pilot experiments with four PDX models (DF68, DF101, DF118, and DF20) to perform power calculation. With eight animals per group, the study was powered to detect a minimum difference of 36% in tumor growth inhibition between conditions, given 80% power, α = 0.05, and a standard deviation of 20%. Tumor response was monitored weekly during treatment using BLI. Tumor-growth rate analysis under different treatment arms was blinded from the investigators. At the end of the treatment, ascites cells were harvested from the peritoneal cavity, collected, lysed with RBC buffer (BioLegend), and pellet volume was measured before snap freezing. To monitor treatment

tolerability, body weights were monitored every 4 days. Solid tumors and ascites cells from all the mice were also formalin fixed for IHC analysis.

Histology and IHC analysis of PDXs

IHC for cleaved caspase-3 was carried out using paraffin sections of formalin-fixed tissue by deparaffinization, treatment with antigen retrieval buffer (Citrate pH6, Sigma) and incubation with anticleaved caspase-3 primary antibody (Cell Signaling Technology, CST 9661). Bound antibody was detected using a secondary anti-rabbit (SignalStain Boost, Cell Signaling Technology) followed by 3,3′-diaminobenzidine staining (DAB, Sigma), and sections were counterstained with hematoxylin. A customized Cell Profiler pipeline was written to automatically identify the percentage of cleaved caspase-3–positive tumor cells. The RGB images were split in different channels generating two images to identify nuclei (hematoxylin) and cleaved caspase-3–positive cells (DAB). Each image was converted into a binary image, and a threshold was applied to select pixels with a defined intensity. The area occupied by pixels in each image was measured. Cell death index was calculated as the ratio of cleaved caspase-3–positive area over nuclei area. We used at least 20 locations per PDX model per treatment arm across different mice. For the scoring of the solid tumor implants in the peritoneal cavity of PDXs, sections were stained with hematoxylin and eosin. A pathologist blinded to the experiments reviewed the slides. A score was assigned to each tumor based on the size of the tumor: 1 for small, 2 for medium, and 3 for big tumor. A score of 1 was also assigned to tumor cellular aggregates visible in the section. A sum of the scores was calculated and indicated as tumor implants score for each treatment group.

Copy-number variation, reverse phase protein array (RPPA), Western blot, BIM knockdown, and qPCR analysis

Copy-number variation analysis for the MEK/ERK pathway was performed by quantifying alterations in *BRAF*, *KRAS*, and *NF1* of the TCGA tumors. Copy-number values were reported as ratios of the PDX sample to a reference normal value and were $\log_2$ transformed for further analysis. Thresholds were used to define alterations as follows: (i) amplification ≥ 0.5; (ii) low-level gain ≤ 0.25; (iii) heterozygous deletion ≤ -0.25; (iv) homozygous deletion ≤ -0.5. Genomic sequencing of the PDX models, including sample library construction, targeted capture, next-generation sequencing, and bioinformatics analyses were performed as previously described (27, 30, 31). In brief, fragmented genomic DNA from the PDX models were used for targeted regions using the Agilent SureSelect 50 Mb kit according to the manufacturer's instructions (Agilent). DNA sequencing data will be available from the European Genome-phenome Archive, (Accession number: EGAS00001003427). Captured DNA libraries were sequenced with the Illumina HiSeq 2000 Genome Analyzer (Illumina). Sequence reads were analyzed and aligned to the human genome sequence (hg18) with Eland v.2 algorithm in CASAVA 1.7 software (Illumina). Potential somatic mutations and copy-number alterations were identified using VariantDx software as previously described (PMID: 25877891, 26416732, and 27573169). Potential alterations were compared with mouse sequences from experimentally obtained mouse targeted sequence data as well as the reference mouse genome (mm9) to remove mouse-specific variants. Mutations of interest were visually inspected in PDX sequences using Integrative Genomics

Viewer, version 2.3.23. Protein lysates were extracted from short-term *in vitro* and orthotopic *in vivo* PDX samples. For the RPPA assay, 40 µg of protein lysate per sample was analyzed. Protein lysates were extracted from short-term *in vitro* and orthotopic *in vivo* PDX samples. The list of measured proteins included 308 unique antibodies, and protein measurements were assessed at MD Anderson RPPA Core. Heat maps were generated using GraphPad Prism and Java TreeView. In the different experiments, $\log_2$ transformation and median centering were performed whenever indicated. For the analysis of TCGA samples, data were collected from the TCPA portal (http://tcpaportal.org/). $\log_2$-transformed and median centered values were used, and unsupervised hierarchical clustering was performed using Cluster software. For the analysis of the PDX models, MEK/ERK pathway score was calculated by summing all the values of the indicated proteins. Western blotting experiments were performed using BIM antibody (CST, 2933S), p-BIMS69 (CST, 4585S), p-ERKT202/T204 (Sigma, M9692), total ERK (CST, 9102S), cleaved caspase-3 (CST, 9661L); NOXA (CST, 14766S); PUMA (CST, 4976S); β-actin (Sigma, A1978). For BIM knockdown experiments, siRNA oligos from Dharmacon were used (L-004383-00-0005). For qPCR, RNA was extracted from short-term *in vitro* PDX cells treated with GDC-0973. cDNA was synthesized using the Quanta Qscript cDNA synthesis kit (VWR), and primers for *BIM* and *GAPDH*, as housekeeping gene, were used in Power SYBR Green PCR Mix (Life Technology): *BIM* R-TGGCAAAG-CAACCTTCTGA; F-GGCCCCAGGTCTGAGC; *GAPDH* R-ATGGG-GAAGGTGAAGGTCG; F-GGGGTCATTGATGGCAACAATA.

Statistical analysis

Correlation between IC_{50} values and protein expression levels of each of the 308 proteins assayed by RPPA either before or after drug treatment was assessed using Pearson correlation in GraphPad Prism. Pearson r coefficient was used to identify proteins with positive (negative r) and negative (positive r) correlation with drug sensitivity. To adjust for multiple comparisons we used the false discovery rate approach (method of Benjamini–Hochberg; ref. 32) and reported q values. Linear regression models were generated using IC_{50} values as the outcome variable and RPPA expression values as predictors with the *lm* function in R 3.4.2. For multiple regression, statistical significance was assessed with likelihood ratio tests of nested models from the *lrtest* package and a threshold of $P < 0.05$. For all the other experiments, significance was assessed using two-tailed Student t test unless otherwise stated. P values below 0.05 were considered significant; their magnitude is given in the text and/or figure legends and asterisks in the figures mark level of significance.

Results

The MEK/ERK pathway is activated in a subset of HGSOC PDX models

Proteomic analysis of TCGA tumor samples by RPPA revealed that the MEK/ERK pathway is commonly activated in a subset of HGSOC (7). To further assess activation of the ERK pathway in HGSOC, we compared the relative activation of ERK in HGSOC TCGA tumors by assessing its state of phosphorylation. The data show that there are relatively higher levels of phosphorylated ERK (pERK) in a large subset of HGSOC samples (Fig. 1A). Importantly, in this analysis, the levels of pERK strongly correlate with the levels of phosphorylation of its upstream regulators, MEK1
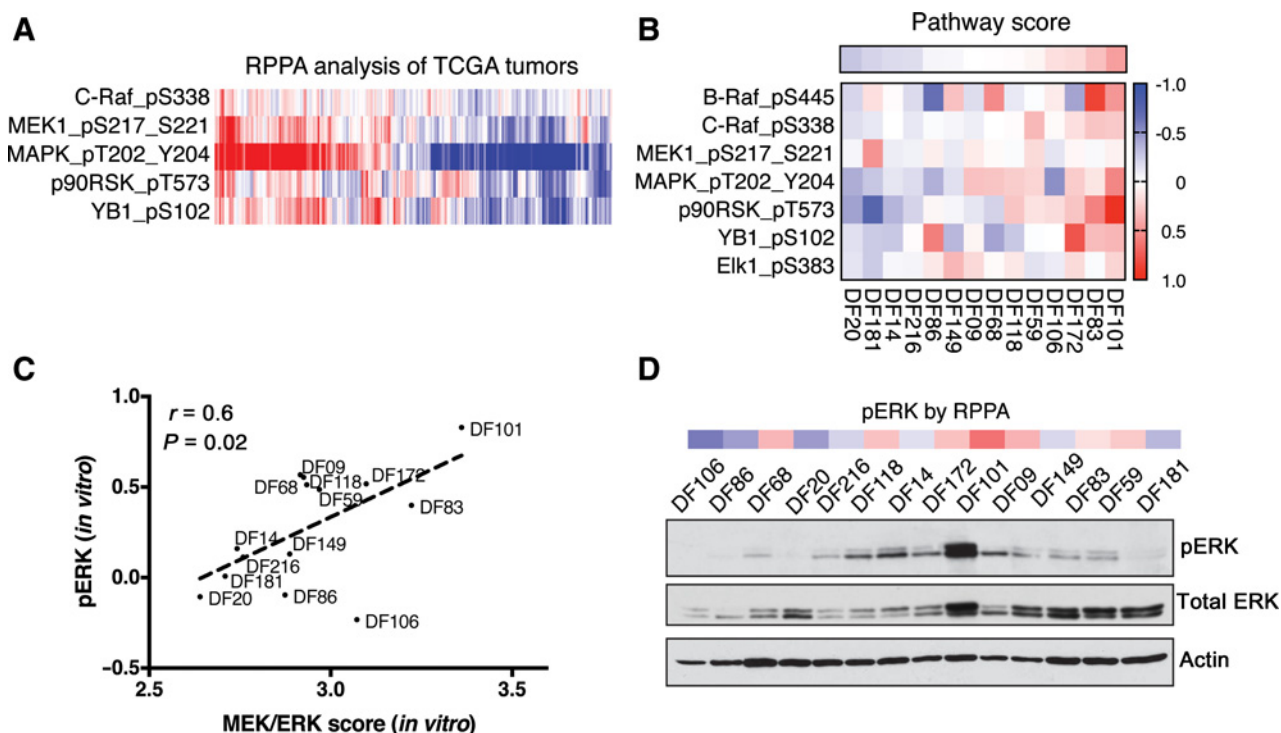
Figure 1.
HGSOC PDX models exhibit a range of activation of the MEK/ERK pathway. **A,** Heat map showing protein levels (log$_2$-transformed, median-centered) of MEK/ERK pathway proteins in HGSOC tumors from TCGA ($n = 285$). Data were obtained from TCPA portal (http://tcpaportal.org/). Samples were hierarchically clustered using Cluster software as described in Materials and Methods. **B,** Heat map showing protein levels (log$_2$-transformed, median-centered) of MEK/ERK pathway proteins in PDX ascites cells under short-term *in vitro* culture conditions. Samples are ranked according to the MEK/ERK pathway activation score calculated as described in Materials and Methods. Data are representative of two independent experiments. **C,** Correlation analysis of pERK levels and MEK/ERK activation score (Pearson $r = 0.6$, $P = 0.02$). **D,** Western blot analysis of pERK in PDX ascites cells cultured *in vitro* in lysates from **B**. The levels of pERK from the RPPA analysis in **B** are shown for comparison.

and RAF, and its downstream target p90RSK and its target pYB1, providing strong evidence of pathway activation. Because mutations in Ras pathway genes are not common in HGSOC, the elevated levels of MEK/ERK pathway activation in HGSOC is most likely due to upstream activation of this pathway through other pathway drivers, e.g., receptor tyrosine kinases.

To assess whether the MEK/ERK pathway is a potential vulnerability in HGSOC, we systematically analyzed the extent of pathway activation and the effect of its inhibition in a panel of well-annotated HGSOC PDX models. These models were generated from ascites/pleural effusions from patients with advanced disease and have been profiled for copy-number alterations, RNA expression and RPPA proteomic analysis (27). All the PDX models carried mutations in *TP53*, which is mutated in the vast majority of HGSOC (Supplementary Table S1). Although most of the PDX models do not harbor amplifications or deletions that would be predicted to be associated with activation of the MEK/ERK pathway, two PDX models (DF20 and DF118) harbor homozygous deletion of *NF1* (a RAS GTPase activating protein), one has a mutation in *KRAS* (DF216), some have gains of *KRAS* and/or *BRAF* or heterozygous deletions of *NF1* (Supplementary Fig. S1A). Because mutations in the genes of the MEK/ERK pathway that occur in HGSOC do not predict the activation of the pathway in tumor samples, we measured the relative activation status at the protein level using RPPA on lysates of short-term *in vitro* cultures of ascites cells from the PDX models. We previously described a

workflow for the harvest and culture of these cells (referred to here as PDX ascites cells) for *in vitro* drug-sensitivity studies and molecular characterization (29). We measured the protein levels of several members of the MEK/ERK pathway, including upstream positive activators (pRAF, pMEK1, and pERK) and downstream targets (pp90RSK, pYB-1, and pElk1), and calculated a pathway activation score by adding the values of all these proteins (as described previously; ref. 7). Figure 1B shows a heat map of the 14 PDX models, ranked based on pathway score and the relative levels of phosphorylation of MEK/ERK pathway components, and demonstrates the extent to which pathway activation varies across the models. The pathway activation score correlates with the level of activated pERK measured by RPPA (Fig. 1C). In addition, relative levels of pERK detected by Western blotting are similar to those measured by RPPA (Fig. 1D). The pathway activation scores of short-term *in vitro* cultures were generally similar to those of their corresponding xenografts grown orthotopically in mice (*in vivo*; Supplementary Fig. S1B). These results confirm that the MEK/ERK pathway is activated in a subset of HGSOC PDX models and that PDX ascites cells can be utilized to interrogate the importance of this pathway in HGSOC.

MEK inhibition does not affect cell viability but upregulates the proapoptotic protein BIM *in vitro*

To determine the response of the 14 PDX models to MEK pathway inhibition, we performed dose-response studies with the

Iavarone et al.
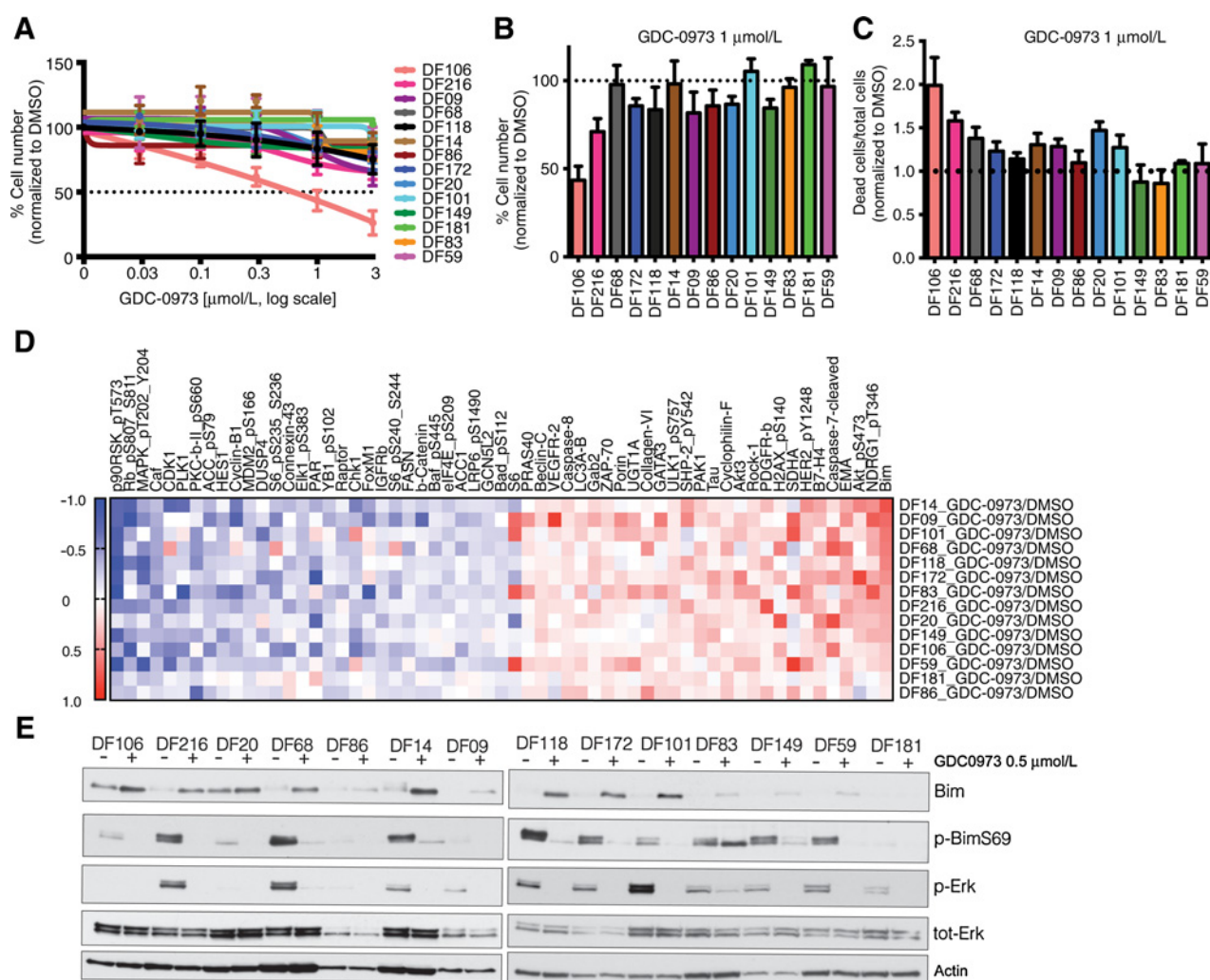
Figure 2.
Sensitivity and proteomic adaptive response to MEK inhibition in HGSOC PDX models *in vitro*. **A,** Five-point dose-response curves of 14 HGSOC PDX ascites cells treated with increasing concentrations of GDC-0973 for 96 hours *in vitro*. Cell number was measured by luciferase assay and data were normalized to DMSO control. Each data point represents mean ± SEM of three independent experiments. Each experiment was performed with six technical replicates. **B,** Relative cell number of all the PDX ascites cells treated with 1 μmol/L GDC-0973 for 96 hours. Data were derived from dose-response curves in **A**. **C,** Analysis of cell death induced by 1 μmol/L of GDC-0973 drug combination 96 hours after drug exposure. Dead cells were detected by staining with NucGreen dye (Invitrogen) and cells were counted using laser scanning cytometry. Data are representative of two independent experiments, and error bars are SEM (*n* = 4 wells). **D,** PDX ascites cells were treated with 0.5 μmol/L GDC-0973 for 48 hours *in vitro*, and protein lysates were harvested and analyzed by RPPA. The heat map shows the proteins with the largest fold increases (red) or decreases (blue) relative to DMSO after treatment with GDC-0973 across all 14 PDX samples. Data are mean log$_2$-transformed values for three technical replicates, representative of two independent experiments. **E,** Western blot of BIM, p-BimS69, pERK, and total ERK levels in protein lysates from PDX ascites cells treated with either vehicle (DMSO) or 0.5 μmol/L GDC-0973 for 48 hours. Actin was used as a loading control.

potent and highly selective MEK inhibitor GDC-0973 (cobimetinib), which is FDA approved for *BRAF*-mutated melanoma in combination with the BRAF inhibitor vemurafenib (33, 34). The PDX models were previously engineered to express a firefly luciferase reporter to monitor cell numbers *in vitro* and tumor growth *in vivo* (27). The PDX ascites cells were treated with clinically relevant doses of GDC-0973 (35, 36) for 96 hours *in vitro*, and luciferase assay was used as a readout of cell number. We found that GDC-0973 treatment had minimal effects on cell number (Fig. 2A and B; Supplementary Fig. S2A), with only two PDX models, DF106 and DF216, displaying a substantial reduction. These two models showed the most significant GDC-0973-

induced increase in cell death, indicating that the reduction in cell number is predominantly due to cell death (Fig. 2C). Interestingly, DF216 is the model with a *KRAS* mutation.

To assess the extent of MEK pathway inhibition and subsequent adaptive response, we performed RPPA on samples before and after treatment with GDC-0973. The 14 PDX ascites cells were treated with a fixed concentration of GDC-0973 (0.5 μmol/L), and 308 proteins were analyzed by RPPA after 48 hours of treatment. Figure 2D shows a heat map of the 30 most downregulated (blue) and upregulated (red) proteins across all 14 PDX models. Treatment with GDC-0973 significantly reduced the phosphorylation of ERK and its target p90RSK, and this was

confirmed by Western blot analysis (Fig. 2E). The fold change in pERK correlated with the extent of baseline activation of the pathway (Supplementary Fig. S2B). The RPPA analysis showed a slight reduction in cell proliferation markers (p-Rb and Cyclin B1), consistent with a reduction in cell number in some models. The most upregulated phosphoprotein was MEK, consistent with inhibition of its catalytic activity, its phosphorylation by RAF proteins, and activation of feedback loops (37). Upregulation of the proapoptotic protein BIM was detected by RPPA (Fig. 2D) and Western blotting in almost all of the models (Fig. 2E). The MEK pathway regulates BIM expression at both the transcriptional and protein stability levels. Activated ERK1/2 phosphorylates BIM on serine 69, leading to its ubiquitination and degradation (38, 39). In addition, ERK1/2-mediated phosphorylation of FOXO3A promotes its degradation and thus inhibits FOXO3A-dependent transcription of BIM (40).

We also measured *BIM* mRNA before and after MEK inhibition and found that *BIM* transcription is increased compared with untreated cells consistent with stabilization of FOXO3A (Supplementary Fig. S2C). Because the balance of pro- and antiapoptotic proteins dictates whether a cell undergoes apoptosis, we also assessed the fold changes in protein levels of other BCL-2 family members after MEK inhibition and found that, with the exception of BIM, the vast majority of the other pro- or antiapoptotic proteins were not affected by MEK inhibition (Supplementary Fig. S2D). Because PUMA and NOXA were not included in the RPPA analysis, we analyzed their levels by Western blotting and found no significant changes in protein levels after GDC-0973 treatment (Supplementary Fig. S2F).

Taken together, these findings demonstrate that MEK inhibition upregulates the level of the proapoptotic protein BIM, suggesting that MEK inhibition may increase priming of tumor cells to undergo apoptosis.

MEK inhibition induces apoptotic priming and sensitizes cells to BCL-2/X$_L$ inhibition in HGSOC PDX models *in vitro*

The inability of MEK inhibition to affect cell number suggested that the induction of BIM alone is not sufficient to induce cell killing and that concomitant suppression of one or more antiapoptotic proteins is necessary to induce tumor cell death. The antiapoptotic members of the BCL-2 family, including BCL-2 and BCL-X$_L$, exert their survival functions by binding and neutralizing the apoptotic effectors BAX and BAK. We have previously demonstrated that the 14 PDX models express different levels of the BCL-2 family proteins and show a wide range of sensitivity to the dual BCL-2/X$_L$ inhibitor ABT-737 (29). To assess whether the apoptotic priming induced by MEK inhibition could be exploited therapeutically, we assessed the effects of GDC-0973 in combination with the orally available BCL-2/X$_L$ inhibitor ABT-263 (navitoclax), which has been clinically evaluated in several different tumor types, including ovarian cancer (41–43). We performed *in vitro* dose-response studies in the 14 PDX models with ABT-263 alone or in a 1:1 fixed ratio with GDC-0973. As we previously reported, ABT-263 alone caused a variable reduction in cell number, with half of the models showing IC$_{50}$s in the range of 0.1–0.3 μmol/L (Fig. 3A; Supplementary Fig. S3A). Interestingly, combination of ABT-263 and GDC-0973 was more effective in decreasing cell number than single agents in 10 of the 14 PDX models (Figure 3B; Supplementary Fig. S3A). These results were not specific to GDC-0973, as other MEK inhibitors, such as PD0325901 and MEK162

(44, 45), showed similar efficacy in reducing cell numbers when combined with ABT-263 (Supplementary Fig. S3B). IC$_{50}$ calculations revealed that there is up to 8-fold increased sensitivity to the GDC-0973 and ABT-263 drug combination compared with ABT-263 alone (e.g., DF101; Fig. 3C). Drug synergy was assessed using the Bliss-independence model (46, 47), which does not require IC$_{50}$ values for all samples since treatment with GDC-0973 did not yield IC$_{50}$ values for most PDX models. The Bliss score is the difference between the calculated inhibition value if the two agents act independently and the observed combined inhibition values. Figure 3D shows the Bliss scores for each of the five dose combinations tested and the average across all combinations. Positive Bliss scores indicate that the combination effect is greater than additive (synergistic). The results show that GDC-0973 and ABT-263 combination is synergistic in the majority of the PDX models. Among the models that showed the lowest average Bliss score were those that were very sensitive to ABT-263 as a single agent (i.e., DF68, DF216, and DF86) and those with the least reduction in cell number after treatment with the drug combination (DF181, DF59, and DF149; Fig. 3B).

We next evaluated the cell killing effects of the single agents and the drug combination after 96 hours of treatment. As described in Fig. 2, GDC-0973 increased cell death significantly only in two models (DF106 and DF216). The GDC-0973 and ABT-263 combination induced a significant increase in cell death compared with single-agent ABT-263 in most of the responsive models (Fig. 3E). Cell death induction was validated in a subset of PDX ascites cells that exhibit a range of sensitivities to the drug combination by immunoblotting for cleaved caspase-3 after 48 hours of treatment *in vitro* (Supplementary Fig. S3C). Concurrent treatment with a pan-caspase inhibitor in a subset of PDX models reduced the sensitivity of the drug combination and rescued the cell killing effect, confirming that cell death is occurring through induction of the intrinsic apoptosis pathway (Fig. 3F; Supplementary Fig. S3D).

Although ABT-263 targets both BCL-2 and BCL-X$_L$, we have previously reported greater dependency on BCL-X$_L$ versus BCL-2 for survival in these HGSOC PDX models (29). Therefore, we investigated the sensitivity of these PDX ascites cells to specific inhibitors of BCL-2 or BCL-X$_L$ as single agents and in combination with GDC-0973. We found that treatment with the BCL-X$_L$-specific inhibitor (A-1155463) alone or in combination with GDC-0973 phenocopied the effects of ABT-263, whereas treatment with the BCL-2-specific inhibitor (ABT-199/venetoclax) had no effect on any of the PDX models tested (Supplementary Fig. S3E and S3F), confirming that BCL-X$_L$, and not BCL-2, plays a major role in cell survival in these PDX models.

We have previously shown that the PDX models most resistant to GDC-0973 and ABT-263 (DF149, DF83, DF181, and DF59) express the high levels of MCL-1 (29). To examine the contribution of MCL-1 to the resistance to combined GDC-0973 and ABT-263 treatment, we concurrently treated the cells with GDC-0973, ABT-263, and an MCL-1 inhibitor (A-1210477). MCL-1 inhibition significantly increased the efficacy of combined GDC-0973 and ABT-263 treatment, indicating that the antiapoptotic protein MCL1 plays a role in the survival of these PDX models (Supplementary Fig. S3G).

Taken together, these results demonstrate that inhibition of the MEK pathway results in apoptotic priming of HGSOC PDX models and increases their dependency specifically on BCL-X$_L$ for survival. As a result, combined inhibition of MEK and BCL-X$_L$

Iavarone et al.
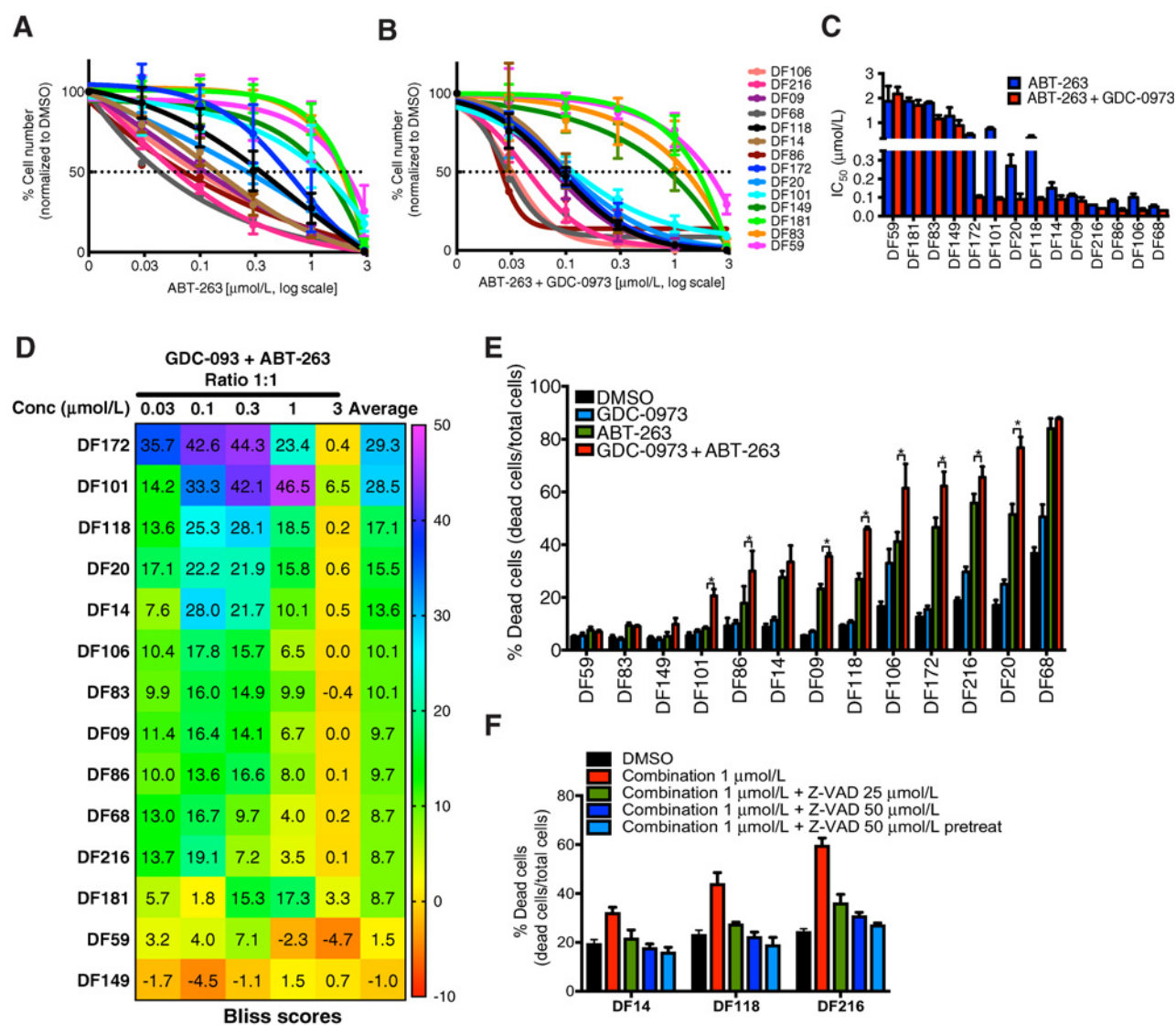
Figure 3.
Combined inhibition of MEK and BCL-2/X_L is synergistic and induces cell death in HGSOC PDX models *in vitro*. **A** and **B,** Dose-response curves of 14 HGSOC PDX ascites cells treated with ABT-263 alone (**A**) or in fixed ratio combination with GDC-0973 (**B**) for 96 hours. Cell number was measured by luciferase assay, and data are normalized to DMSO control. Data, mean ± SEM of three independent experiments. Each experiment was performed with six technical replicates. **C,** IC$_{50}$ of ABT-263 alone or in combination with GDC-0973. Data are derived from the experiments in A and **B.** Bars, mean ± SEM of three independent experiments. **D,** Bliss score calculated for each of the dose combinations of GDC-093 and ABT-263 across the 14 PDX models. The dose-response data of GDC-0973 alone are derived from Fig. 2A. These experiments were performed at the same time. The average of the Bliss score across the 5 doses is also reported. For Bliss score calculation details, see Materials and Methods. Data are derived from experiment in **A** and **B,** and Bliss score represents the mean of three independent experiments. **E,** Analysis of cell death induced by single agents and the ABT-263 plus GDC-0973 drug combination 96 hours after drug exposure (1 μmol/L of each drug). Dead cells were detected as described in Fig. 2C. Data are representative of two independent experiments, and error bars are SEM ($n = 4$ wells). DF181 was excluded from this analysis because it showed green autofluorescence that interfered with the NucGreen dye used to detect dead cells. *, $P < 0.05$. **F,** Analysis of cell death induced by ABT-263 plus GDC-0973 drug combination (1 μmol/L of each drug) in the presence of the pan-caspase inhibitor Z-VAD-FMK as indicated. Pretreatment with 50 μmol/L of Z-VAD-FMK was performed 24 hours before the addition of ABT-263 plus GDC-0973. Dead cells were detected as in Fig. 2C. Data are representative of two independent experiments, and error bars are SEM ($n = 4$ wells).

acts synergistically to decrease cell number and increase apoptotic cell death in HGSOC PDX ascites cells *in vitro*.

Combination of MEK and BCL-2/X_L inhibition reduces tumor growth *in vivo*

We next investigated whether the combined inhibition of MEK and BCL-2/X_L is effective in reducing tumor burden in HGSOC

PDX models *in vivo*. First, we selected four PDX models that displayed sensitivity to the drug combination *in vitro* based on IC$_{50}$ (DF68, DF118, DF20, and DF101) to conduct a pilot survey of the *in vivo* efficacy of the combination therapy. Ascites cells were injected intraperitoneally into immunocompromised mice, allowed to grow for 2 to 3 weeks depending on the PDX model, and then treated daily for 21 days with GDC-0973 (7.5 mg/kg)

and ABT-263 (100 mg/kg), a dosing schedule that was tolerated in non–tumor-bearing mice. Tumor burden was measured by BLI during the course of treatment and by harvesting ascites cells and measuring cell volume at the endpoint. In all PDX models tested, we observed a reduction in tumor growth by at least 50% when GDC-0973 was combined with ABT-263 compared with vehicle control mice (Supplementary Fig. S4A). This result was in concordance with the *in vitro* sensitivity data.

Based on these preliminary results, we compared the effects of the GDC-0973 and ABT-263 drug combination to single agents in two PDX models (DF118 and DF20) that were sensitive to the drug combination in the *in vivo* efficacy pilot experiment described above and in which a synergistic effect was observed *in vitro* (Fig. 3D). Single-agent treatment with either GDC-0973 or ABT-263 reduced tumor growth by 50% in DF118, but did not affect tumor growth in DF20. Combined GDC-0973 and ABT-263 treatment significantly reduced tumor growth in both models compared with single agents or vehicle (Fig. 4A–C; Supplementary Fig. S4B). The drug treatments were tolerated as indicated by minimal changes in animal body weight in both PDX models (Fig. 4D).

We next evaluated whether the combination treatment was effective in reducing the burden of solid peritoneal tumor masses in the abdominal cavity of mice. Histologic analysis revealed that the drug combination caused nearly complete eradication of tissue-disseminated solid tumor implants in the DF118 mice compared with vehicle and single-agent treatments (Fig. 4E). Although we did observe some residual tissue-disseminated solid tumor implants in DF20 mice after treatment with the drug combination, they displayed larger areas of necrosis compared with other treatments groups (Supplementary Fig. S4C), suggesting that these remaining solid tumor implants are unlikely to be viable. To evaluate whether the combination treatment induced apoptotic cell death *in vivo* in DF20 solid tumor implants, we performed IHC of cleaved caspase-3 (CC3). Quantification of representative images revealed that the combination treatment significantly increased cell death compared with single-agent treatments (Fig. 4F).

These data demonstrate that the GDC-0973 and ABT-263 combination substantially reduces tumor burden in HGSOC PDX models compared with untreated controls and to each agent alone at tolerable doses. These results also corroborate the use of short-term *in vitro* cultures of the HGSOC PDX models for predicting drug sensitivity *in vivo*. Although tumor regression was not observed in this short-term tumor model, this reduction in tumor growth is significant for the chemoresistant tumor models.

BIM protein levels before and after MEK inhibition correlate with sensitivity to combined inhibition of MEK and BCL-2/X_L

The range of responses elicited by the GDC-0973 and ABT-263 combination across the 14 PDX models (Fig. 3B and C) presented a valuable opportunity to identify markers of drug responsiveness. We performed linear correlation analysis to evaluate correlations between the IC_{50} of the drug combination and the 308 proteins measured by RPPA in the PDX models before treatment. Using a false-discovery rate approach to correct for multiplicity analysis, we identified a total of 16 proteins that significantly correlate with drug response (Table 1). One of the top positive predictors was BIM ($R^2 = 0.51$, $P = 0.004$; q value = 0.15; Fig. 5A). This result indicates that PDX models with high basal expression of BIM respond better to the drug combination than those with

low BIM expression. Indeed, all six PDX models with high BIM expression had lower IC_{50} values for the drug combination indicating greater sensitivity. However, among the eight PDX models with low expression of BIM, there was a subset of four PDX models (DF09, DF118, DF172, and DF101) that also displayed lower IC_{50} values and were sensitive to the drug combination, suggesting that, in this specific subset of PDX models, BIM baseline levels are insufficient to fully explain the response.

Because BIM was identified as one of the most upregulated proteins following MEK inhibition, we next investigated whether the changes in BIM can predict response to the drug combination to a greater extent than baseline BIM levels. We analyzed the correlation between BIM levels after treatment with GDC-0973 (measured by RPPA) and IC_{50} values for the drug combination. We found that the correlation between IC_{50} and BIM levels after GDC-0973 treatment is better than that of baseline BIM, with an R^2 of 0.71 ($P = 0.0001$; Fig. 5B). Interestingly, BIM was the only protein among the positive predictors whose predictive power increased after treatment with GDC-0973 (Supplementary Fig. S5A). Of the eight PDX models with low basal BIM, the four sensitive ones (with low IC_{50}; DF09, DF118, DF172, and DF101) show upregulation of BIM following MEK inhibition (Supplementary Fig. S5B), providing mechanistic insights into the responsiveness of these models. In contrast, the four resistant PDX models (with high IC_{50}; DF181, DF59, DF83, and DF149) show minimal upregulation of BIM after treatment with GDC-0973 (Supplementary Fig. S5B). These results were confirmed in an independent set of established HGSOC ovarian cancer cell lines ($n = 9$). We performed dose-response experiments with the GDC-0973 and ABT-263 combination, calculated IC_{50} values, and performed correlation analysis between IC_{50} and BIM expression after treatment with GDC-0973. We found that BIM levels after MEK inhibition correlate with response to the drug combination ($R^2 = 0.54$; $P = 0.02$; Supplementary Fig. S5C).

To investigate the functional role of BIM in drug responsiveness, we performed siRNA knockdown experiments in two PDX models, DF14 and DF101, that express high BIM protein levels following MEK inhibition and display two different levels of synergy with combined MEK and BCL-2/X_L inhibition (Figs. 2E; 5A and B). siRNA knockdown decreased BIM protein levels by 40% and 80% in DF14 and DF101, respectively (Fig. 5C), and reduced the sensitivity to the GDC-0973 and ABT-263 combination as indicated by the increase of the IC_{50} values (Fig. 5D). These results were validated in the ovarian cancer cell line OAW28 that expresses high levels of BIM (Supplementary Fig. S5D).

The ability to upregulate BIM in response to MEK inhibition likely contributes significantly to the differential sensitivity of GDC-0973 and ABT-263 drug combination in those PDX models with low basal BIM levels (DF09, DF118, DF172, DF101 vs. DF181, DF59, DF83, and DF149). To identify proteomic markers that distinguish these PDX models with low basal BIM, we examined the proteins that were differentially expressed between the responders (DF09, DF118, DF172, and DF101) and the nonresponders (DF181, DF59, DF83, and DF149). We identified pERK as one of the differentially expressed proteins ($P = 0.04$; Fig. 5E). Indeed, the PDX models with low basal BIM expression that are sensitive to the drug combination also show higher expression of pERK compared with the models that are poor responders (Fig. 5E). We also found that the basal levels of pERK can predict the extent to which BIM is upregulated following

Iavarone et al.
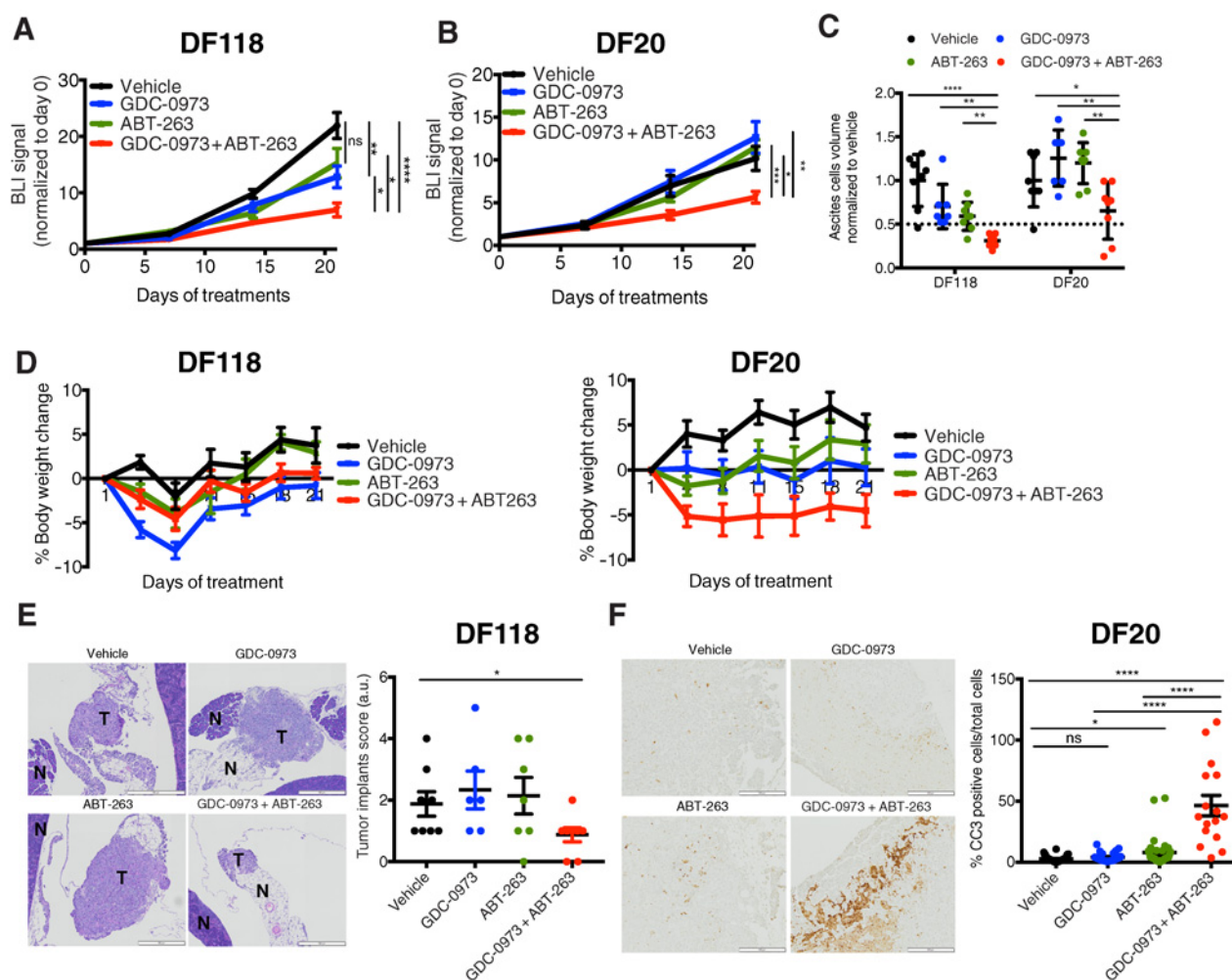
Figure 4.
Combination of MEK and BCL-2/X$_L$ inhibition reduces tumor burden compared with single agents in HGSOC PDX models *in vivo*. **A** and **B,** Tumor growth curves determined by BLI of two PDX models, DF118 (**A**) and DF20 (**B**), treated with GDC-0973 (7.5 mg/kg QD) and ABT-263 (100 mg/kg QD) alone or in combination for 21 days. $n = 8$ mice per treatment arm. Data are normalized to BLI signal before treatment (day 0). Error bars, SEM. Statistical significance assessed with unpaired two-tailed *t* test: *, $P \leq 0.02$; **, $P < 0.02$; ****, $P < 0.0001$. **C,** Analysis of endpoint (day 21) ascites volume of the two PDX models. Data are normalized to vehicle control mice. Error bars, SEM. $n = 8$ per treatment arm. Statistical significance assessed with an unpaired two-tailed *t* test: *, $P < 0.04$; **, $P < 0.004$; ***, $P < 0.002$. **D,** Changes in animal body weight for each treatment group ($n = 8$ per group; error bars are SEM). **E,** Representative histologic images of solid tumor implants in the abdominal cavity of mice implanted with the DF118 PDX model (left). T = tumors; N = normal mouse tissues. Scale bar, 500 μm. Blinded quantification of solid tumor implants (right) was performed by a pathologist. A score was assigned to each tumor implant, and the presence of circulating tumor cells in the peritoneal cavity was also noted. The scoring method is described in Materials and Methods. Briefly, a score was assigned to each tumor based on the size of the tumor: 1 for small, 2 for medium and 3 for large tumor. A score of 1 was assigned also in the case of tumor cell aggregates visible in the section. Statistical significance was assessed with an unpaired two-tailed *t* test: *, $P < 0.05$. **F,** Representative cleaved caspase-3 (CC3) IHC images of tumor implants from the DF20 PDX model (left). Scale bar, 200 μm. Quantification of CC3 staining (right) performed as indicated in Materials and Methods section. Error bars represent SEM across at least 20 locations within tumor implants from three mice per treatment group. Statistical significance assessed with an unpaired two-tailed *t* test: *, $P < 0.02$; ****, $P < 0.0001$.

MEK inhibition ($R^2 = 0.62$; $P = 0.02$; Fig. 5F), indicating that PDX models displaying higher activation of ERK respond by upregulating BIM to a greater extent than the PDX models with low ERK activation. Finally, multiple regression analysis revealed that a model that includes both baseline levels of BIM and pERK correlates better with response to dual inhibition than a model that includes just BIM (model improvement, $P = 0.04$; Supplementary Fig. S5E and S5F), suggesting that both baseline markers could be used to correlate response to combination therapy.

Together, these results demonstrate that baseline BIM expression represents a candidate marker of responsiveness to combined inhibition of MEK and BCL-2/X$_L$. However, BIM expression after treatment with single-agent MEK inhibitor has a higher predictive power than basal BIM expression, suggesting that BIM upregulation is a critical component of responsiveness to this combination therapy. Importantly, we also show that the extent of BIM upregulation after MEK inhibition can be predicted by the expression of baseline pERK in HGSOC PDX models.

Table 1. Pearson correlation analysis of 308 proteins with IC_{50} to GDC-0973 and ABT-263 drug combination in 14 PDX models

Proteins	r coefficient	R^2	P value	q value
Positive correlations				
IGFBP2	−0.9343	0.8729	0.0001	0.0306
Bim	−0.7175	0.5148	0.0039	0.1492
PAK1	−0.6877	0.473	0.0066	0.1938
Smad4	−0.668	0.4462	0.009	0.1938
Gab2	−0.6646	0.4417	0.0095	0.1938
XPF	−0.6598	0.4353	0.0102	0.1951
Negative correlations				
PRAS40	0.6658	0.4202	0.0093	0.1938
Rab11	0.667	0.4449	0.0092	0.1938
Lck	0.6745	0.455	0.0081	0.1938
eEF2	0.6959	0.4843	0.0057	0.1938
C-Raf	0.7229	0.1647	0.0035	0.1492
EGFR_pY1173	0.7253	0.7046	0.0033	0.1492
MEK1	0.7654	0.3554	0.0014	0.0857
Atg3	0.7834	0.6137	0.0009	0.0689
COG3	0.8235	0.6781	0.0003	0.0306
EGFR	0.8394	0.5261	0.0002	0.0306

Discussion

In this study, we examined adaptive responses to inhibition of the MEK/ERK pathway, which is upregulated in a large portion of HGSOC (5, 6, 15–17), in a panel of HGSOC PDX models. We identified vulnerabilities of drug-treated tumor cells that could be targeted to enhance the efficacy of inhibitors of this pathway and demonstrate the effectiveness of a drug combination targeting MEK and the antiapoptotic proteins BCL-2 and BCL-X_L. In addition, we identify protein markers that correlate with the effectiveness of this drug combination in chemoresistant HGSOC PDX models and established ovarian cancer cells. Given the high frequency of the development of chemoresistance in HGSOC and the need for orthogonal approaches to treat refractory disease, this drug combination warrants evaluation for the treatment of chemoresistant HGSOC.

Despite strong activation of the MEK/ERK pathway in multiple PDX models, MEK pathway inhibition elicited minimal effects on cell survival *in vitro* in the majority of the models. Our results are consistent with published reports showing modest preclinical and clinical activity of MEK inhibitors when used as single agents in other tumor types (24, 48). However, in this study, we successfully exploited the apoptotic priming induced by MEK inhibition upregulation of BIM to promote cytotoxicity of the HGSOC models through combined BCL-2/X_L inhibition by ABT-263. This drug combination effectively enhanced cell death *in vitro* and *in vivo* compared with single-agent treatments. The mechanism of BIM regulation by the MEK pathway and the cytotoxic effects of combined MEK and BCL-2/X_L inhibition has been demonstrated in other tumor types characterized by point mutations in RAS/MEK pathway components (49–51), prompting the evaluation of this combination therapy in clinical trials comprising different types of *KRAS*- or *NRAS*-mutated tumors (Clinicaltrial. gov identifiers NCT02079740 and NCT01989585). Our study provides a rationale for inclusion of HGSOC, where activation of the MEK signaling pathway and apoptotic priming following its inhibition is apparent despite the lack of recurrent activating MEK/ERK pathway mutations.

In addition to BIM upregulation, we also detected increased levels of γ-H2AX following MEK inhibition. This finding is consistent with a recent report that showed regulation of DNA-

damage repair pathway by the MEK/ERK pathway in ovarian cancer cell lines, supporting the development of MEK and PARP inhibitor combinations for ovarian cancer (52). We also detected activation of receptor tyrosine kinase signaling, specifically activated HER2, which is in agreement with a dynamic reprogramming of the kinome in response to MEK inhibition that has been reported in triple-negative breast cancer (48). Finally, the AKT pathway was also upregulated following MEK inhibition in the PDX models. Numerous preclinical studies in other tumor types have demonstrated that multiple points of cross-talk, negative feedback, and redundancy exist between the RAS/MEK and the PI3K/AKT pathways and that inhibition of both is crucial to induce tumor cell death (35, 53, 54). However, in initial clinical trials, combining MEK and AKT inhibitors elicited overlapping monotherapy toxicities (55), limiting the clinical utility of this combination. Because we were most interested in new combination therapies that could be imminently translated into the clinic, we did not further pursue this drug combination.

The GDC-0973 and ABT-263 combination therapy that we evaluated was well tolerated in mice, even with concomitant continuous daily dosing of both drugs. Furthermore, both therapeutic agents are currently being evaluated in clinical trials, facilitating immediate translation of our findings to the clinic. GDC-0973 (cobimetinib) is a highly selective, allosteric MEK1/2 inhibitor with generally acceptable tolerability and safety profile in clinical trials. Based on the promising results of a phase III clinical trial (coBRIM), the FDA approved GDC-0973 in 2015 for its utility in combination with vemurafenib in patients with advanced BRAF^{V600}-positive melanomas (34). The oral BCL-2/X_L dual inhibitor ABT-263 (navitoclax) exhibits an acceptable safety profile in clinical trials of patients with solid tumors, with dose-dependent thrombocytopenia as the major adverse effect (56). In this study and a previous one from our lab, we demonstrate that inhibition of BCL-2/X_L as a single agent elicited a wide range of responses in the panel of HGSOC PDX models (29, 57), but when combined with either MEK or PI3K/mTOR inhibitors, it effectively increased cell killing, providing a strong rationale for further evaluation of these combinations in dedicated HGSOC trials. Additionally, by using selective inhibitors of BCL-2 and BCL-X_L inhibitors, we show that BCL-X_L inhibition is sufficient to mediate the cell killing in both these combination therapies, uncovering specific apoptotic vulnerabilities of HGSOC PDX models that can be therapeutically exploited.

The PDX models used here exhibit a range of responses to the combined inhibition of MEK and BCL-2/XL, highlighting the utility of this model system to identify proteins that can be further evaluated as predictors of response. Overall, the results of our correlation analyses are consistent with the model depicted in Fig. 5G. High pretreatment levels of BIM protein predict a strong response to MEK and BCL-2/X_L combined inhibition. However, PDX models in which BIM is low basally, but induced by MEK inhibition, also respond well to MEK plus BCL-2/X_L inhibition. PDX models with low BIM before and after MEK inhibition are poorly responsive.

BIM represents a critical regulator of apoptosis induced by a variety of targeted therapies in both hematologic and solid tumors, including ovarian cancer, as previously demonstrated by our group and others (58). These studies have demonstrated that many therapies that inhibit oncogenic kinase signaling cascades ultimately lead to the inhibition of downstream pathways, including MEK/ERK and PI3K/AKT, and modulate the expression

Iavarone et al.
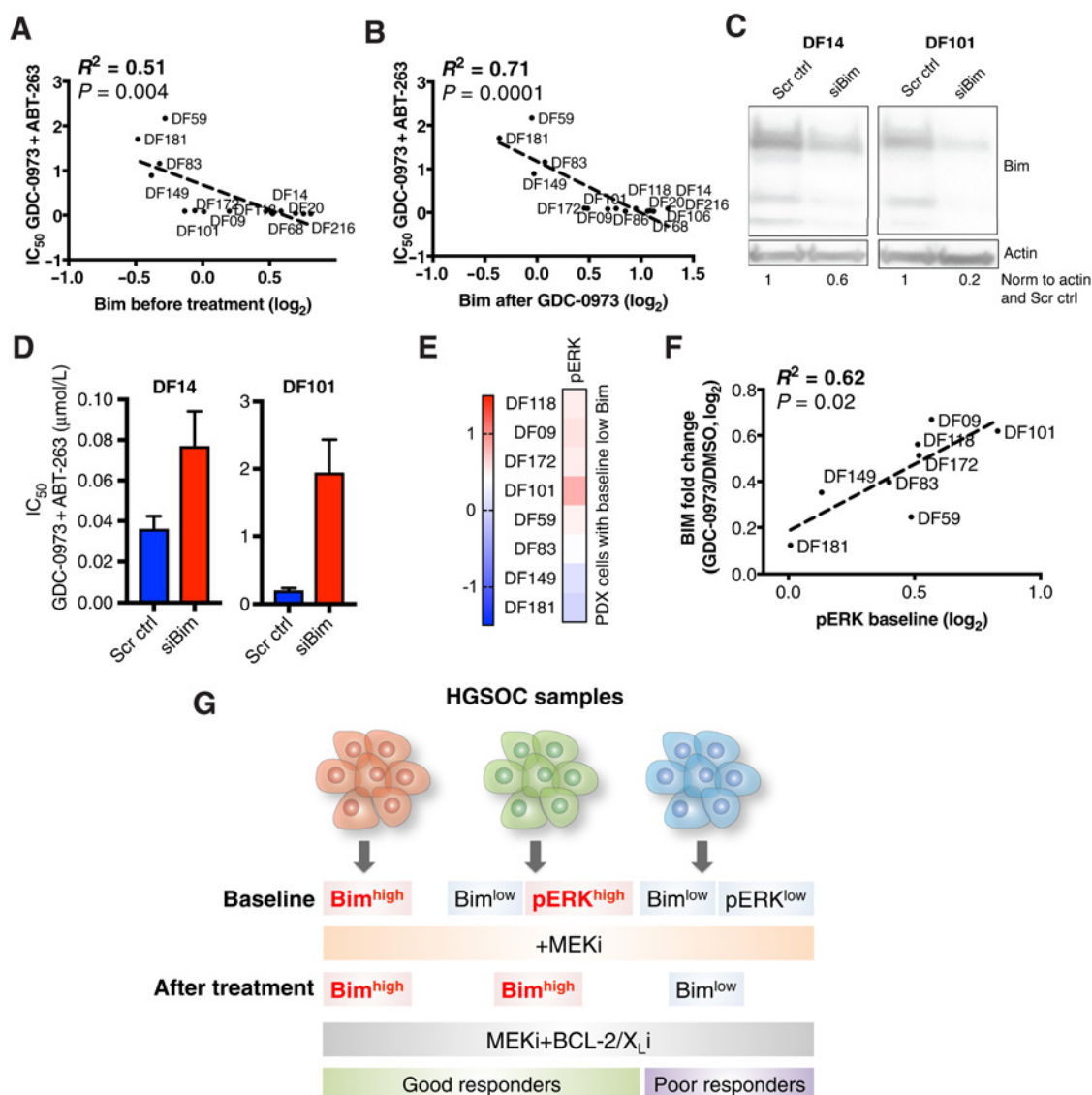
Figure 5.
BIM levels before and after MEK inhibition predicts sensitivity and correlates with levels of activated ERK. **A** and **B,** Linear correlation of BIM expression measured by RPPA before (**A**) and after (**B**) MEK inhibition and IC_{50} values for the GDC-0973 and ABT-263 drug combination in all the 14 PDX models ($P \leq 0.05$, two-tailed). **C,** Western blot of BIM levels after 72 hours of siRNA knockdown in DF14 and DF101. Actin was used as a loading control, and BIM levels are normalized to scramble control (Scr ctrl). **D,** IC_{50} to GDC-0973 and ABT-263 drug combination after 72 hours of BIM knockdown in DF14 and DF101. **E,** Heat map of basal pERK levels measured by RPPA before treatment in the PDX models with low expression of BIM ($P \leq 0.05$). Values are log_2-transformed. **F,** Linear correlation of baseline levels of pERK and fold-induction of BIM after MEK inhibition in the PDX models with low baseline BIM expression. Values are log_2-transformed ($P \leq 0.05$, two-tailed). **G,** Model to predict response to MEK and BCL-2/X_L combination therapy in HGSOC samples using biomarkers before and after treatment.

of BIM, suggesting that this mechanism is indeed critical for the therapy-induced cell killing. Our group has demonstrated that direct inhibition of either MEK or PI3K pathways induced expression of BIM in PDX models of HGSOC and increased priming of the cancer cells to apoptotic cell death regulated by the BCL-2 family proteins (29). These studies corroborate the importance of the BIM regulatory axis in maintaining the survival state of HGSOC. Our work here demonstrates that BIM levels not only correlate with therapy response, but also play a functional role in the response, in that depletion of BIM is able to reduce the

sensitivity of PDX cells to the drug combination. Furthermore, our results suggest that there is a threshold level of BIM upregulation after MEK inhibition that the PDXs with low baseline BIM must reach in order to be committed to death and therefore respond to the combination therapy.

The evidence that BIM correlates with response to treatment with GDC-0973 and ABT-263 has important implications for the design of clinical trials to evaluate the MEK and BCL-2/X_L combination therapy. Measuring BIM levels after the start of treatment would be useful not only to select a larger number of

patients who are likely to benefit from this combination therapy but also to mitigate unnecessary treatment for those patients predicted to respond poorly. Applying this approach in the clinic remains a challenge, as it would require measuring BIM protein levels in tumor biopsies before and during therapy. Although the identification of posttreatment biomarkers and their incorporation into clinical trials are at their infancy, this represents a promising approach to improve treatment response prediction in patients.

Considering the challenges of evaluating posttreatment biomarkers in the clinical setting, we performed additional analyses to identify other molecular features that can be evaluated before treatment and can predict the extent of BIM upregulation after MEK inhibition. We found that the baseline level of activated ERK (pERK) correlates with BIM fold induction after MEK inhibition in PDX models with low baseline BIM levels. Additionally, through a multiple regression analysis, we demonstrate that a predictive statistical model that includes both baseline BIM and pERK levels has a better predictive power than one that includes BIM alone.

Additional work is needed to uncover the molecular mechanism that mediates BIM suppression in the PDX models that show poor response to MEK and BCL-2/X$_L$ combination therapy. Epigenetic mechanisms have been implicated in BIM suppression in different tumor types, suggesting that a combination with epigenetic agents might be effective in these models. Furthermore, because MCL-1 contributes to resistance to combined MEK–BCL2/XL inhibition, it is important to develop therapeutic strategies to inhibit MCL-1 for treatment of tumors with high levels of this protein.

In conclusion, our study sets the stage to evaluate the effectiveness of combined inhibition of MEK and BCL-2/X$_L$ and whether MEK inhibition–induced BIM or pretreatment levels of BIM and pERK correlate with response in HGSOC patients.

Disclosure of Potential Conflicts of Interest

Authors' Contributions

Acknowledgments

References

1. Matulonis UA, Sood AK, Fallowfield L, Howitt BE, Sehouli J, Karlan BY. Ovarian cancer. Nat Rev Dis Primers 2016;2:16061.
2. Siegel RL, Miller KD, Jemal A. Cancer statistics, 2019. A Cancer J Clin 2019; 69:7–34.
3. Berns EMJJ, Bowtell DD. The changing view of high-grade serous ovarian cancer. Cancer Res 2012;72:2701–4.
4. Bowtell DD, Böhm S, Ahmed AA, Aspuria P-J, Bast RC, Beral V, et al. Rethinking ovarian cancer II: reducing mortality from high-grade serous ovarian cancer. Nat Rev Cancer 2015;15:668–79.
5. Bell D, Berchuck A, Birrer M, Chien J, Cramer DW, Dao F, et al. Integrated genomic analyses of ovarian carcinoma. Nature 2011;474: 609–15.
6. Patch A-M, Christie EL, Etemadmoghadam D, Garsed DW, George J, Fereday S, et al. Whole-genome characterization of chemoresistant ovarian cancer. Nature 2015;521:489–94.
7. Akbani R, Ng PKS, Werner HMJ, Shahmoradgoli M, Zhang F, Ju Z, et al. A pan-cancer proteomic perspective on The Cancer Genome Atlas. Nat Commun 2014;5:3887.
8. Li J, Lu Y, Akbani R, Ju Z, Roebuck PL, Liu W, et al. TCPA: a resource for cancer functional proteomics data. Nat Methods 2013;10:1046–7.
9. Yap TA, Omlin A, de Bono JS. Development of therapeutic combinations targeting major cancer signaling pathways. J Clin Oncol 2013;31: 1592–605.
10. Liu J, Matulonis UA. New strategies in ovarian cancer: translating the molecular complexity of ovarian cancer into treatment advances. Clin Cancer Res 2014;20:5150–6.
11. Liu JF, Barry WT, Birrer M, Lee J-M, Buckanovich RJ, Fleming GF, et al. Combination cediranib and olaparib versus olaparib alone for women with recurrent platinum-sensitive ovarian cancer: a randomised phase 2 study. Lancet Oncol 2014;15:1207–14.

12. Kim H, George E, Ragland R, Rafial S, Zhang R, Krepler C, et al. Targeting the ATR/CHK1 axis with PARP inhibition results in tumor regression in BRCA-mutant ovarian cancer models. Clin Cancer Res 2017;23: 3097–108.

13. Matulonis UA, Wulf GM, Barry WT, Birrer M, Westin SN, Farooq S, et al. Phase I dose escalation study of the PI3kinase pathway inhibitor BKM120 and the oral poly (ADP ribose) polymerase (PARP) inhibitor olaparib for the treatment of high-grade serous ovarian and breast cancer. Ann Oncol 2017;28:512–8.

14. Holohan C, Van Schaeybroeck S, Longley DB, Johnston PG. Cancer drug resistance: an evolving paradigm. Nat Rev Cancer 2013;13:714–26.

15. Schwarz RF, Ng CKY, Cooke SL, Newman S, Temple J, Piskorz AM, et al. Spatial and temporal heterogeneity in high-grade serous ovarian cancer: a phylogenetic analysis. PLoS Med 2015;12:e1001789.

16. Hew KE, Miller PC, El-Ashry D, Sun J, Besser AH, Ince TA, et al. MAPK activation predicts poor outcome and the MEK inhibitor, selumetinib, reverses antiestrogen resistance in ER-positive high-grade serous ovarian cancer. Clin Cancer Res 2016;22:935–47.

17. Zhang H, Liu T, Zhang Z, Payne SH, Zhang B, McDermott JE, et al. Integrated proteogenomic characterization of human high-grade serous ovarian cancer. Cell 2016;166:755–65.

18. Macintyre G, Goranova T, De Silva D, Ennis D, Piskorz AM, Eldridge M, et al. Copy-number signatures and mutational processes in ovarian carcinoma. biorxiv 2018;50:1262–70.

19. Zhao Y, Adjei AA. The clinical development of MEK inhibitors. Nat Rev Clin Oncol 2014;11:385–400.

20. Miller CR, Oliver KE, Farley JH. MEK1/2 inhibitors in the treatment of gynecologic malignancies. Gynecol Oncol 2014;133:128–37.

21. Pepa Della C, Tonini G, Santini D, Losito S, Pisano C, Di Napoli M, et al. Low grade serous ovarian carcinoma: from the molecular characterization to the best therapeutic strategy. Cancer Treat Rev 2015;41:136–43.

22. Okumura S, Jänne PA. Molecular pathways: the basis for rational combination using MEK inhibitors in KRAS-mutant cancers. Clin Cancer Res 2014;20:4193–9.

23. Johnson GL, Stuhlmiller TJ, Angus SP, Zawistowski JS, Graves LM. Molecular pathways: adaptive kinome reprogramming in response to targeted inhibition of the BRAF-MEK-ERK pathway in cancer. Clin Cancer Res 2014; 20:2516–22.

24. Farley J, Brady WE, Vathipadiekal V, Lankes HA, Coleman R, Morgan MA, et al. Selumetinib in women with recurrent low-grade serous carcinoma of the ovary or peritoneum: an open-label, single-arm, phase 2 study. Lancet Oncol 2013;14:134–40.

25. Domcke S, Sinha R, Levine DA, Sander C, Schultz N. Evaluating cell lines as tumour models by comparison of genomic profiles. Nat Commun 2013;4: 2126.

26. Scott CL, Becker MA, Haluska P, Samimi G. Patient-derived xenograft models to improve targeted therapy in epithelial ovarian cancer treatment. Front Oncol 2013;3:295.

27. Liu JF, Palakurthi S, Zeng Q, Zhou S, Ivanova E, Huang W, et al. Establishment of patient-derived tumor xenograft models of epithelial ovarian cancer for preclinical evaluation of novel therapeutics. Clin Cancer Res 2017;23:1263–73.

28. George E, Kim H, Krepler C, Wenz B, Makvandi M, Tanyi JL, et al. A patient-derived-xenograft platform to study BRCA-deficient ovarian cancers. JCI Insight 2017;2:e89760.

29. Zervantonakis IK, Iavarone C, Chen H-Y, Selfors LM, Palakurthi S, Liu JF, et al. Systems analysis of apoptotic priming in ovarian cancer identifies vulnerabilities and predictors of drug response. Nat Commun 2017;8:365.

30. Jones S, Anagnostou V, Lytle K, Parpart-Li S, Nesselbush M, Riley DR, et al. Personalized genomic analyses for cancer mutation discovery and interpretation. Sci Transl Med 2015;7:283ra53–3.

31. Bertotti A, Papp E, Jones S, Adleff V, Anagnostou V, Lupo B, et al. The genomic landscape of response to EGFR blockade in colorectal cancer. Nature 2015;526:263–7.

32. Benjamini Y, Hochberg Y. Controlling the false discovery rate: a practical and powerful approach to multiple testing. J R Stat Soc 1995;57:289–300.

33. Larkin J, Ascierto PA, Dréno B, Atkinson V, Liszkay G, Maio M, et al. Combined vemurafenib and cobimetinib in BRAF-mutated melanoma. N Engl J Med 2014;371:1867–76.

34. Ascierto PA, McArthur GA, Dréno B, Atkinson V, Liszkay G, Di Giacomo AM, et al. Cobimetinib combined with vemurafenib in advanced BRAF (V600)-mutant melanoma (coBRIM): updated efficacy results from a randomised, double-blind, phase 3 trial. Lancet Oncol 2016;17: 1248–60.

35. Hoeflich KP, Merchant M, Orr C, Chan J, Otter Den D, Berry L, et al. Intermittent administration of MEK inhibitor GDC-0973 plus PI3K inhibitor GDC-0941 triggers robust apoptosis and tumor growth inhibition. Cancer Res 2012;72:210–9.

36. Choo EF, Belvin M, Boggs J, Deng Y, Hoeflich KP, Ly J, et al. Preclinical disposition of GDC-0973 and prospective and retrospective analysis of human dose and efficacy predictions. Drug Metab Dispos 2012;40: 919–27.

37. Caunt CJ, Sale MJ, Smith PD, Cook SJ. MEK1 and MEK2 inhibitors and cancer therapy: the long and winding road. Nat Rev Cancer 2015;15: 577–92.

38. Luciano F, Jacquel A, Colosetti P, Herrant M, Cagnol S, Pages G, et al. Phosphorylation of Bim-EL by Erk1/2 on serine 69 promotes its degradation via the proteasome pathway and regulates its proapoptotic function. Oncogene 2003;22:6785–93.

39. Ley R, Balmanno K, Hadfield K, Weston C, Cook SJ. Activation of the ERK1/2 signaling pathway promotes phosphorylation and proteasome-dependent degradation of the BH3-only protein, Bim. J Biol Chem 2003;278:18811–6.

40. Yang J-Y, Zong CS, Xia W, Yamaguchi H, Ding Q, Xie X, et al. ERK promotes tumorigenesis by inhibiting FOXO3a via MDM2-mediated degradation. Nat Cell Biol 2008;10:138–48.

41. Oltersdorf T, Elmore SW, Shoemaker AR, Armstrong RC, Augeri DJ, Belli BA, et al. An inhibitor of Bcl-2 family proteins induces regression of solid tumours. Nature 2005;435:677–81.

42. Park C-M, Bruncko M, Adickes J, Bauch J, Ding H, Kunzer A, et al. Discovery of an orally bioavailable small molecule inhibitor of prosurvival B-cell lymphoma 2 proteins. J Med Chem 2008;51:6902–15.

43. Tse C, Shoemaker AR, Adickes J, Anderson MG, Chen J, Jin S, et al. ABT-263: a potent and orally bioavailable Bcl-2 family inhibitor. Cancer Res 2008; 68:3421–8.

44. Barrett SD, Bridges AJ, Dudley DT, Saltiel AR, Fergus JH, Flamme CM, et al. The discovery of the benzhydroxamate MEK inhibitors CI-1040 and PD 0325901. Bioorg Med Chem Lett 2008;18:6501–4.

45. Bendell JC, Javle M, Bekaii-Saab TS, Finn RS, Wainberg ZA, Laheru DA, et al. A phase 1 dose-escalation and expansion study of binimetinib (MEK162), a potent and selective oral MEK1/2 inhibitor. Br J Cancer 2017;116: 575–83.

46. Greco WR, Bravo G, Parsons JC. The search for synergy: a critical review from a response surface perspective. Pharmacol Rev 1995;47:331–85.

47. Lehár J, Stockwell BR, Giaever G, Nislow C. Combination chemical genetics. Nat Chem Biol 2008;4:674–81.

48. Duncan JS, Whittle MC, Nakamura K, Abell AN, Midland AA, Zawistowski JS, et al. Dynamic reprogramming of the kinome in response to targeted MEK inhibition in triple-negative breast cancer. Cell 2012;149:307–21.

49. Cragg MS, Jansen ES, Cook M, Harris C, Strasser A, Scott CL. Treatment of B-RAF mutant human tumor cells with a MEK inhibitor requires Bim and is enhanced by a BH3 mimetic. J Clin Invest 2008;118:3651–9.

50. Corcoran RB, Cheng KA, Hata AN, Faber AC, Ebi H, Coffee EM, et al. Synthetic lethal interaction of combined BCL-XL and MEK inhibition promotes tumor regressions in KRAS mutant cancer models. Cancer Cell 2013;23:121–8.

51. Tan N, Wong M, Nannini MA, Hong R, Lee LB, Price S, et al. Bcl-2/Bcl-xL inhibition increases the efficacy of MEK inhibition alone and in combination with PI3 kinase inhibition in lung and pancreatic tumor models. Mol Cancer Ther 2013;12:853–64.

52. Sun C, Fang Y, Yin J, Chen J, Ju Z, Zhang D, et al. Rational combination therapy with PARP and MEK inhibitors capitalizes on therapeutic liabilities in RAS mutant cancers. Sci Transl Med 2017;9:eaal5148.

53. Engelman JA, Chen L, Tan X, Crosby K, Guimaraes AR, Upadhyay R, et al. Effective use of PI3K and MEK inhibitors to treat mutant Kras G12D and PIK3CA H1047R murine lung cancers. Nat Med 2008;14:1351–6.

54. Tolcher AW, Khan K, Ong M, Banerji U, Papadimitrakopoulou V, Gandara DR, et al. Antitumor activity in RAS-driven tumors by blocking AKT and MEK. Clin Cancer Res 2015;21:739–48.

55. Tolcher AW, Patnaik A, Papadopoulos KP, Rasco DW, Becerra CR, Allred AJ, et al. Phase I study of the MEK inhibitor trametinib in combination with the AKT inhibitor afuresertib in patients with solid tumors and multiple myeloma. Cancer Chemother Pharmacol 2015;75:183–9.

56. Gandhi L, Camidge DR, Ribeiro de Oliveira M, Bonomi P, Gandara D, Khaira D, et al. Phase I study of Navitoclax (ABT-263), a novel Bcl-2 family inhibitor, in patients with small-cell lung cancer and other solid tumors. J Clin Oncol 2011;29:909–16.

57. Lheureux S, N'Diaye M, Blanc-Fournier C, Dugué AE, Clarisse B, Dutoit S, et al. Identification of predictive factors of response to the BH3-mimetic molecule ABT-737: an ex vivo experiment in human serous ovarian carcinoma. Int J Cancer 2015;136: E340–50.

58. Hata AN, Engelman JA, Faber AC. The BCL2 family: key mediators of the apoptotic response to targeted anticancer therapeutics. Cancer Discov 2015;5:475–87.

Molecular Cancer Therapeutics

Combined MEK and BCL-2/X$_L$ Inhibition Is Effective in High-Grade Serous Ovarian Cancer Patient–Derived Xenograft Models and BIM Levels Are Predictive of Responsiveness

Claudia Iavarone, Ioannis K. Zervantonakis, Laura M. Selfors, et al.

Updated version	Access the most recent version of this article at: doi:10.1158/1535-7163.MCT-18-0413
Supplementary Material	Access the most recent supplemental material at: http://mct.aacrjournals.org/content/suppl/2019/01/24/1535-7163.MCT-18-0413.DC1

Cited articles	This article cites 58 articles, 17 of which you can access for free at: http://mct.aacrjournals.org/content/18/3/642.full#ref-list-1

E-mail alerts	Sign up to receive free email-alerts related to this article or journal.
Reprints and Subscriptions	To order reprints of this article or to subscribe to the journal, contact the AACR Publications Department at pubs@aacr.org.
Permissions	To request permission to re-use all or part of this article, use this link http://mct.aacrjournals.org/content/18/3/642. Click on "Request Permissions" which will take you to the Copyright Clearance Center's (CCC) Rightslink site.